

Fault Detection of Rotation Machinery using Periodic Time-Frequency Sparsity*

Yin Ding^{†1}, Wangpeng He^{1,2,3}, Binqiang Chen⁴, Yanyang Zi^{2,3}, and Ivan W. Selesnick¹

¹*Tandon School of Engineering, New York University, 6 Metrotech Center, Brooklyn, NY 11201, USA*

²*State Key Laboratory for Manufacturing and Systems Engineering, Xi'an Jiaotong University, Xi'an, China*

³*School of Mechanical Engineering, Xi'an Jiaotong University, Xi'an, China*

⁴*School of Aeronautics and Astronautics, Xiamen University, Xiamen, China*

July 6, 2022

Abstract

This paper addresses the problem of extracting periodic oscillatory features in vibration signals for detecting faults in rotation machinery. To extract the feature, we propose an approach in the short-time Fourier transform (STFT) domain where the periodic oscillatory feature manifests itself as a relatively sparse grid. To estimate the sparse grid, we formulate an optimization problem using customized binary weights in the regularizer, where the weights are formulated to promote periodicity. As examples, the proposed approach is applied to simulated data, and used as a tool for diagnosing faults in bearings and gearboxes for real data, and compared to some state-of-the-art methods. The results show the proposed approach can effectively detect and extract the periodical oscillatory features.

1 Introduction

Condition monitoring and fault diagnosis of rotating machines are of great importance to prevent machinery breakdown in numerous industrial applications. Vibration signals generated by faults in rotating components have been widely studied. Detecting and extracting transient vibration signatures is of vital importance for vibration-based detection of faults in rotating machinery. However, the observed vibration signals are usually corrupted by very heavy background noise [47, 23]. Many diagnostic techniques have been developed to extract the fault features based on different transforms, such as short time Fourier transform (STFT) [63, 22, 35, 27, 46] and wavelet transform [62, 8, 61, 34, 39, 26, 30, 7, 33]. Some methods use morphological decomposition methods, such as empirical mode decomposition (EMD) [38, 25], or demodulation [52, 40, 59]. Some methods combine conventional time-frequency analysis with other techniques suitable for transients detection, such as bispectrum-based method [20, 14] and spectral kurtosis (SK) based methods [4, 3, 65, 9].

The use of sparse representations for fault detection was initially illustrated in Ref. [63], where basis pursuit denoising (BPD) [12, 13] was adopted to exploit the sparsity of vibration signals in different domains in order to detect and extract fault features. In Ref. [46], the author considered a morphological component

*Preprint

[†]Email: yd372@nyu.edu

analysis (MCA) problem [21, 54, 55], which is a sparsity-based decomposition approach, to improve the extraction of fault features. In Ref. [17] matching pursuit (MP) [43] was used on a customized dictionary to extract oscillatory fault features. In Ref. [29], a sparse representation using the tunable Q-factor wavelet transform [51, 50] is utilized to extract oscillatory fault features. Most recently, sparse coding techniques are introduced for fault feature extraction [57].

The periodicity (also called fault characteristic or fundamental frequency in some cases) of potential fault features is very important information for fault diagnosis. In many cases, this information can be simply obtained using the geometry of the specific components under steady rotating speed, or directly obtained from the user operation manual. It is already required as necessary information in many fault diagnosis methods [62, 40, 56, 58]. Some fault diagnosis methods use periodicity information as a verification step after feature extraction (e.g. [41, 46]), and some methods use it to determine an optimal frequency band when extracting the oscillation frequency of the fault feature [40, 56, 58]. Only a few very recent works use the temporal periodic structure to extract fault features [44, 28].

The overlapping group sparsity (OGS) approach has been discussed in [11, 10], where a multi-dimensional group structure has been modeled in various domains and convex optimization problems have been formulated, to take advantage of group behavior (e.g. coefficients in STFT domain) to recover signals from noisy observations. Using OGS to extract fault features was introduced and formulated as an convex optimization problem in [28], in which the fault features are assumed to be a periodic sequence of pulses. In addition, it was shown that the objective function can be convex even if some specified non-convex penalty functions are used to promote sparsity. Moreover, when the periodicity information is known, a binary-weighted group structure was used in the regularization, capturing the period of the potential fault features.

In this work, we consider the problem wherein the fault features are comprised of a sequence of oscillatory transients, and sparsity should be promoted in the time-frequency domain. The discrete-time vibration observation y is modeled by

$$y = x + w, \tag{1}$$

where x is an approximately-periodic sequence of oscillatory transients where the period is determined by the characteristic frequency of potential faults, and w is additive Gaussian noise. Moreover, we assume that the oscillation frequencies of the transient component x are unknown but relatively consistent over a moderate interval.

Under the signal model, we seek a solution to the optimization problem

$$c^* = \arg \min_c \left\{ F(c) = \frac{1}{2} \|y - Ac\|_2^2 + \lambda \Phi(c) \right\}, \tag{2}$$

for the purpose of extracting the fault feature $x \in \mathbb{R}^N$, where c denotes the coefficients corresponding to an overcomplete transform A of x , where $x = Ac$, and $\lambda > 0$ is a regularization parameter and Φ is a sparsity-promoting penalty function (regularizer) in the domain of c . This paper aims to extract the oscillatory fault features as periodically structured groups of coefficients in the time-frequency domain. We set the operator A to be the normalized inverse STFT, and the function Φ is customized to capture the periodicity in the STFT domain.

Furthermore, in this work, we use a non-convex regularizer to promote sparsity and to enhance the performance of the proposed method. To solve the optimization problem (2), we illustrate an iterative algorithm which is guaranteed to converge.

1.1 Notation

In this paper, the elements of a vector $x \in \mathbb{R}^N$ are denoted as x_n or $[x]_n$, and the norms are defined as

$$\|x\|_1 := \sum_n |x_n|, \quad (3a)$$

$$\|x\|_2^2 := \sum_n |x_n|^2. \quad (3b)$$

The norms of a complex vector $z \in \mathbb{C}^N$ is defined as

$$\|z\|_1 := \sum_n |z_n|, \quad (4a)$$

$$\|z\|_2^2 := \sum_n |z_n|^2, \quad (4b)$$

where the definition of absolute value of a complex number $a \in \mathbb{C}$ is given by

$$|a| := \sqrt{[\operatorname{Re}(a)]^2 + [\operatorname{Im}(a)]^2}. \quad (5)$$

As a consequence, $\|z\|_2^2$ can be written explicitly as

$$\|z\|_2^2 = \sum_n [\operatorname{Re}([z]_n)]^2 + [\operatorname{Im}([z]_n)]^2 \quad (6a)$$

$$= \|z_r\|_2^2 + \|z_i\|_2^2, \quad (6b)$$

where $z = z_r + iz_i$, and $z_r, z_i \in \mathbb{R}^N$ are vectors of the real and imaginary part of z , respectively.

For multi-dimensional matrices, e.g. $B \in \mathbb{R}^{M \times N}$, we denote its elements as $[B]_{m,n}$. We use bold $\mathbf{0}$ and $\mathbf{1}$ to express all 0's and 1's matrices. More specifically, $\mathbf{0}(K, N)$ is a matrix of size $K \times N$, and all its elements are zero, and $\mathbf{1}(K, N)$ is a matrix, the elements of which are all one.

2 Preliminaries

2.1 Majorization-minimization

The majorization-minimization (MM) method [24, 37, 31] simplifies a complicated optimization problem into a sequence of easier ones. To solve a convex optimization problem

$$u^* = \arg \min_u F(u), \quad (7)$$

the MM method is described by iteration

$$u^{(i+1)} = \arg \min_u G(u, u^{(i)}), \quad (8)$$

where $G : \mathbb{R}^N \times \mathbb{R}^N \rightarrow \mathbb{R}$ is a continuously differentiable function, satisfying

$$G(u, v) \geq F(u), \quad \text{for all } u, v, \quad (9a)$$

$$G(u, u) = F(u). \quad (9b)$$

The detailed proof of convergence for convex problems has been given in Ref. [37, Chapter 10].

2.2 Review of BSUM

Block successive upper-bound minimization algorithm (BSUM) is described in [49]. Its original goal is to overcome the uniqueness requirement of block coordinate descent (BCD) method (also known as Gauss-Seidel method) [5, 42]. BSUM is an iterative method to solve optimization problems, which allows the objective function to be non-convex and/or non-smooth. When the objective function is neither convex nor smooth, the algorithm will at least converge to a stationary point under some weak assumptions [49, Theorem 2]. This algorithm has been applied to transceiver design in MIMO multi-cellular communication system, which has a non-convex formulation [48]. In order to facilitate our proposed algorithm, as a short review, we only rewrite a special case of BSUM using our notation.

The problem is defined as

$$x^* = \arg \min_x Q(x), \quad (10)$$

where $Q : \mathbb{R}^N \rightarrow \mathbb{R}$ is continuous and has at least one stationary point. In this case, we slightly relax the definition of ‘optimal solution’, whereas if the objective function is not convex, we allow the ‘optimum’ to be merely a local minimizer. Note that, when function Q is strictly convex, the unique minimizer is the global minimizer, therefore the relaxation of optimal does not affect convex problems, where x^* is still the true global minimizer.

We assume the unknown $x \in \mathbb{R}^N$ can be divided into three blocks: $x_0 \in \mathbb{R}^{N_0}$, $x_1 \in \mathbb{R}^{N_1}$ and $x_2 \in \mathbb{R}^{N_2}$ with $N = N_0 + N_1 + N_2$. Then the objective function Q in (10) can be rewritten using the expression of the three blocks, where the problem is

$$\{x_0^*, x_1^*, x_2^*\} = \arg \min_{x \in \mathbb{R}^N} Q(x_0, x_1, x_2), \text{ where } x = \begin{bmatrix} x_0 \\ x_1 \\ x_2 \end{bmatrix}, \quad (11)$$

and if we can find a continuous function $G : \mathbb{R}^N \times \mathbb{R}^N \rightarrow \mathbb{R}$, which is the block-wise upper-bound of Q , defined as

$$G((x_0, x_1, x_2), (v_0, x_1, x_2)) \geq Q(x_0, x_1, x_2), \quad \text{for all } x \text{ and } v_0 \in \mathbb{R}^{N_0}, \quad (12a)$$

$$G((x_0, x_1, x_2), (x_0, v_1, x_2)) \geq Q(x_0, x_1, x_2), \quad \text{for all } x \text{ and } v_1 \in \mathbb{R}^{N_1}, \quad (12b)$$

$$G((x_0, x_1, x_2), (x_0, x_1, v_2)) \geq Q(x_0, x_1, x_2), \quad \text{for all } x \text{ and } v_2 \in \mathbb{R}^{N_2}, \quad (12c)$$

$$G((x_0, x_1, x_2), (x_0, x_1, x_2)) = Q(x_0, x_1, x_2), \quad \text{for all } x, \quad (12d)$$

then problem (11) can be solved by BSUM by the algorithm illustrated in [49, Figure 2]. For the special case of three blocks, we can write the algorithm explicitly as the steps in Table 1.

The condition (12) implies all the assumptions listed in [49, Assumption 2], which ensures that the algorithm in Table 1 converges, and the mathematical proof of convergence can be found in Section IV of [49]. It is worth noting that the convergence behavior of BSUM does not rely on the convexity of the problem.

Table 1: Block successive upper-bound minimization (BSUM) algorithm with three blocks.

```

initial:  $x \in \mathbb{R}^N$ 
repeat:
   $x_0 = \arg \min_{u_0} G((u_0, x_1, x_2), (x_0, x_1, x_2))$ 
   $x_1 = \arg \min_{u_1} G((x_0, u_1, x_2), (x_0, x_1, x_2))$ 
   $x_2 = \arg \min_{u_2} G((u_0, x_1, u_2), (x_0, x_1, x_2))$ 
end
return:  $x = \{x_0, x_1, x_2\}$ 

```

3 SALMA

Split augmented Lagrangian shrinkage algorithm (SALSA) [2] is a recently developed method for solving convex optimization problems. As an efficient ℓ_1 -norm regularized convex problem solver, it has been widely used to solve various signal processing problems [45, 50]. SALSA adopts variable splitting technique and the concept of alternating direction method of multipliers (ADMM) [6, 19], achieving a very simply structured and efficient iterative algorithm. In this section, we propose an algorithm formulated very similar to SALSA. However, in contrast to SALSA, the proposed method converges when used to solve non-convex problems. Because we use the concept of majorization-minimization (MM) in the proposed algorithm, it is termed split augmented Lagrangian majorization-minimization algorithm (SALMA), and can be stated as the following theorem.

Theorem 1. *For optimization problem*

$$x^* = \arg \min_{x \in \mathbb{R}^N} F_0(x) + F_1(x), \quad (14)$$

where function $F_0 : \mathbb{R}^N \rightarrow \mathbb{R}$ and $F_1 : \mathbb{R}^N \rightarrow \mathbb{R}$ are both finite and continuously differentiable, if a function $G_1 : \mathbb{R}^N \times \mathbb{R}^N \rightarrow \mathbb{R}$ majorizes F_1 , i.e., satisfying

$$G_1(u, v) \geq F_1(u), \quad \text{for all } u, v \in \mathbb{R}^N, \quad (15)$$

$$G_1(u, u) = F_1(u), \quad (16)$$

can be found, and it enables the following iterative algorithm

$$u^{(i+1)} = \arg \min_u G_1(u, u^{(i)}) + \frac{\mu}{2} \|u - x - d\|_2^2, \quad (17a)$$

$$x^{(i+1)} = \arg \min_x F_0(x) + \frac{\mu}{2} \|u - x - d\|_2^2, \quad (17b)$$

$$d^{(i+1)} = d^{(i)} - (u - x) \quad (17c)$$

having unique solution at each step, then the algorithm (17) will converge, and converges to a local minimizer of problem (14).

Proof. By introducing a variable $u \in \mathbb{R}^N$ and adding an equality constraint, we can split the variable x , and

then problem (14) is equivalent to

$$\begin{aligned} \{x^*, u^*\} &= \arg \min_{x, u} \left\{ F(x, u) = F_0(x) + F_1(u) \right\} \\ &\text{subject to } x - u = 0. \end{aligned} \quad (18)$$

This problem has an augmented Lagrangian

$$L_A(x, u, \beta) = F(x, u) + \beta^\top(u - x) + \frac{\mu}{2} \|u - x\|_2^2, \quad (19)$$

where $\beta \in \mathbb{R}^N$, and $\mu > 0$. Moreover, we assume that L_A in (19) is finite when x, u, β are all finite, and the saddle point $L_A(x^*, u^*, \beta^*)$ exists and should be finite. This implies that the saddle point (x^*, u^*, β^*) is at least a local minimizer of problem (18). If function $G_1 : \mathbb{R}^N \times \mathbb{R}^N \rightarrow \mathbb{R}$ is continuously differentiable and majorizes [is an upper-bound satisfying (15)] of F_1 , then an upper-bound of L_A can be found as

$$G_A((x, u, \beta), (x, v, \gamma)) = F_0(x) + G_1(u, v) + G_2((x, u, \beta), \gamma) + \frac{\mu}{2} \|u - x\|_2^2, \quad (20)$$

where $G_2((x, u, \beta), \gamma)$ is an upper-bound of $\beta^\top(u - x)$, defined as

$$G_2((x, u, \beta), \gamma) := \beta^\top(u - x) + \frac{1}{2\mu} \|\beta - \gamma\|_2^2 \geq \beta^\top(u - x), \quad \text{for all } \beta, \gamma \in \mathbb{R}^N. \quad (21)$$

Note that G_A in (20) satisfies the block-wise upper-bound conditions listed in (12), when vectorizing $\{x, u, \beta\}$ as a single variable. Hence, BSUM for three blocks (Table 1) can be directly applied to find the stationary point of L_A . Moreover, since L_A goes to extrema only when $\{x, u, \beta\}$ goes to extrema, BSUM will converge to a non-extremal stationary point of L_A , which is the saddle point (see convergence analysis in Ref. [49]).

As a consequence, we can write the algorithm in Table 1 explicitly ‘minimizing’ L_A in (19), and it will converge to a saddle point of L_A ,

$$u^{(i+1)} = \arg \min_u G_1(u, u^{(i)}) + \beta^\top(u - x) + \frac{\mu}{2} \|u - x\|_2^2, \quad (22a)$$

$$x^{(i+1)} = \arg \min_x F_0(x) + \beta^\top(u - x) + \frac{\mu}{2} \|u - x\|_2^2, \quad (22b)$$

$$\beta^{(i+1)} = \arg \min_\beta \beta^\top(u - x) + \frac{1}{2\mu} \|\beta - \beta^{(i)}\|_2^2 \quad (22c)$$

where the step (22c) can be solved explicitly as

$$\beta^{(i+1)} = \beta^{(i)} + \mu(u - x). \quad (23)$$

Similar to SALSAs, we can reorganize the steps by introducing a variable $d \in \mathbb{R}^N$, and then after simple variable substitutions (same to change ALM/MM version I to version II in Section II of Ref. [2]), solving (22) for $\{x^*, u^*\}$ turns out to be iteratively computing the steps illustrated in (17). \square

Note that the algorithm (17) has two steps identical to SALSAs, and the difference is in the sub-problem (17a), where the cost function is based on a continuously differentiable majorizer of F_1 . In contrast to SALSAs, the proposed method will converge when the objective function is not convex, because it is actually a special case of BSUM.

In other words, the proposed algorithm utilizes a Gauss-Seidel procedure to solve a majorization-minimization

(MM) problem. This leads us to term the algorithm SALMA (split augmented Lagrangian majorization-minimization algorithm), which combines SALSA and majorization-minimization methods.

4 Proposed method

4.1 Smoothed penalty function

In this work, we use smoothed penalty function $\phi_\epsilon : \mathbb{R} \rightarrow \mathbb{R}_+$ to induce sparsity, which is a smoothed version of $\phi : \mathbb{R} \rightarrow \mathbb{R}_+$ in Table 2. It is defined as:

$$\phi_\epsilon(u; a) := \phi(\sqrt{u^2 + \epsilon}; a), \quad \epsilon > 0, \quad (24)$$

where ϕ is the non-smooth penalty function satisfies the following properties:

1. $\phi(u; a)$ is continuous on \mathbb{R} .
2. $\phi(u; a)$ is twice continuously differentiable on $\mathbb{R} \setminus \{0\}$.
3. $\phi(u; a)$ is even symmetric: $\phi(u) = \phi(-u)$.
4. $\phi(u; a)$ is increasing and concave on \mathbb{R}_+ .
5. $\phi(u; a) = |x|$, when $a = 0$.

Several typical examples of ϕ are given in Table 2. Figure 1(a-b) gives two specific examples of ϕ in dashed line, and corresponding smoothed versions with $\epsilon = 0.01$ in solid line.

In this work, we use the smoothed penalty function ϕ_ϵ instead of ϕ , because after the smoothing, the function is continuously differentiable on $u \in \mathbb{R}$, and we can easily find the corresponding majorizer,

$$g(u, v) := \frac{u^2}{2\psi(v)} - \underbrace{\left(\frac{v^2}{2\psi(v)} - \phi_\epsilon(v; a) \right)}_{\text{only depends on } v}. \quad (25)$$

where $\psi(v) := v/\phi'_\epsilon(v; a)$, and $g(u, v)$ is quadratic in u . In Ref. [18], the same smoothed penalty functions are used and a detailed proof is given to show that when ϕ satisfies the above 5 conditions, the majorizer (25) satisfies

$$g(u, v) \geq \phi_\epsilon(u; a), \quad \text{for all } u, v, \quad (26a)$$

$$g(u, u) = \phi_\epsilon(u; a). \quad (26b)$$

Figure 1(cd) illustrates the majorizer g of two penalty functions when $v = 0.5$. Note that g never goes to extrema (i.e. $\pm\infty$) if u and v are both finite. Table 2 provides four examples of smoothed penalty functions. Among all these functions, only the first one ('abs') is convex, and the rest are all non-convex. In (24), ϕ is not differentiable at 0, but ϕ_ϵ is differentiable, and when $\epsilon \rightarrow 0$, function $\phi_\epsilon \approx \phi$, but preserving the differentiability at the origin. In practice, we recommend to set ϵ very small, e.g. 10^{-8} .

Table 2: Sparsity-promoting penalty functions.

Penalty	$\phi(u; a)$	$\phi_\epsilon(u; a)$	$\psi(u) = u/\phi'_\epsilon(u; a)$
abs ($a = 0$)	$ u $	$\sqrt{u^2 + \epsilon}$	$\sqrt{u^2 + \epsilon}$
log	$\frac{1}{a} \log(1 + a u)$	$\frac{1}{a} \log(1 + a\sqrt{u^2 + \epsilon})$	$\sqrt{u^2 + \epsilon} (1 + a\sqrt{u^2 + \epsilon})$
rat	$\frac{ u }{1 + a u /2}$	$\frac{\sqrt{u^2 + \epsilon}}{1 + a\sqrt{u^2 + \epsilon}/2}$	$\sqrt{u^2 + \epsilon} (1 + a\sqrt{u^2 + \epsilon})^2$
atan	$\frac{2}{a\sqrt{3}} \left(\tan^{-1} \left(\frac{1 + 2a u }{\sqrt{3}} \right) - \frac{\pi}{6} \right)$	$\frac{2}{a\sqrt{3}} \left(\tan^{-1} \left(\frac{1 + 2a\sqrt{u^2 + \epsilon}}{\sqrt{3}} \right) - \frac{\pi}{6} \right)$	$\sqrt{u^2 + \epsilon} (1 + a\sqrt{u^2 + \epsilon} + a^2(u^2 + \epsilon))$

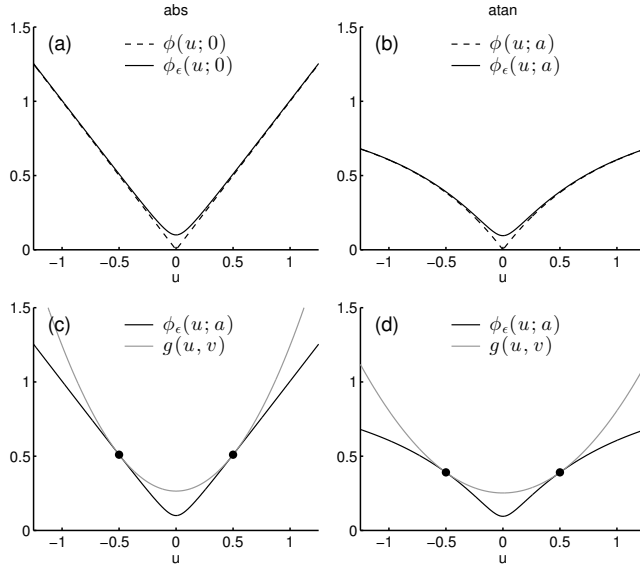


Figure 1: (a) ℓ_1 -norm penalty function and its smoothed version, and (b) arctangent penalty function and its smoothed version, and (c) Majorizer (gray) of the smoothed penalty function in (a). (d) Majorizer (gray) of the smoothed penalty function in (b). For all the figures we set $\epsilon = 0.01, v = 0.5, a = 1$.

4.2 Problem definition

To estimate a sequence of oscillatory transients modeled by (1), through an optimization problem prototyped by (2), we further formulate the optimization problem explicitly as

$$c^* = \arg \min_c \left\{ P(c) = \frac{1}{2} \|y - Ac\|_2^2 + \lambda \sum_{m_1, m_2} \phi_\epsilon(\theta(c, B, m_1, m_2); a) \right\} \quad (27)$$

where $y \in \mathbb{R}^N$, $c \in \mathbb{C}^{M_1 \times M_2}$ are STFT coefficients, and the matrix $A : \mathbb{C}^{M_1 \times M_2} \rightarrow \mathbb{C}^N$ here denotes the inverse short-time Fourier transform operator. When a local optimal of problem (27) is obtained, component x (periodic sequence of oscillatory transients) in signal model (1) is given by

$$\hat{x} = Ac^* \quad (28)$$

In problem (27), we defined the regularizer by function $\theta : \mathbb{C}^{M_1 \times M_2} \times \mathbb{R}^{K_1 \times K_2} \times \mathbb{Z} \times \mathbb{Z} \rightarrow \mathbb{R}$,

$$\theta(c, B, m_1, m_2) = \left[\sum_{k_1=0}^{K_1-1} \sum_{k_2=0}^{K_2-1} [B]_{k_1, k_2} [c]_{m_1+k_1, m_2+k_2}^2 \right]^{1/2}, \quad (29)$$

which is similar to a 2-D convolution. Note that $B \in \mathbb{R}^{K_1 \times K_2}$ is a two-dimensional binary-valued mask describing the group structure, which is to be determined beforehand by the time-frequency information of x and the STFT.

We use \odot to denote element-wise multiplication, so the function θ can be written as a weighted norm of a segment of STFT coefficient c ,

$$\theta(c, B, m_1, m_2) := \|B \odot S(c, m_1, m_2)\|_2. \quad (30)$$

Here $S(c, m_1, m_2)$ denotes a $K_1 \times K_2$ segment of matrix $c \in \mathbb{C}^{M_1 \times M_2}$, where the first element (up and left) is $[c]_{m_1, m_2}$. Moreover, since c is a complex-valued array, where $c = c_r + ic_i$, it follows that,

$$\|B \odot S(c, m_1, m_2)\|_2^2 = \|B \odot S(c_r, m_1, m_2)\|_2^2 + \|B \odot S(c_i, m_1, m_2)\|_2^2 \quad (31)$$

where $S(c_r, m_1, m_2), S(c_i, m_1, m_2) \in \mathbb{R}^{K_1 \times K_2}$ are the corresponding arrays of the real and imaginary parts of $S(c, m_1, m_2)$. Then, in implementation, the real and imaginary parts of the problem can be calculated separately as real values.

For problem (27), in order to capture the known periodicity of x as modeled in (1), we further define binary weighting vectors $b_1 \in \{0, 1\}^{K_1}$ and $b_2 \in \{0, 1\}^{K_2}$ in the following structure,

$$b_1 = \mathbf{1}(1, K_1) = \underbrace{[1, 1, \dots, 1]}_{K_1} \quad (32a)$$

$$\begin{aligned} b_2 &= [\mathbf{1}(1, N_1), \mathbf{0}(1, N_0), \mathbf{1}(1, N_1), \mathbf{0}(1, N_0), \dots, \mathbf{1}(1, N_1)] \\ &= [\underbrace{1, 1, \dots, 1}_{N_1}, \underbrace{0, 0, \dots, 0}_{N_0}, \underbrace{1, 1, \dots, 1}_{N_1}, \underbrace{0, 0, \dots, 0}_{N_0}, \dots, \underbrace{1, 1, \dots, 1}_{N_1}], \end{aligned} \quad (32b)$$

where b_2 captures the feature periodicity with a periodic binary structure, so that the binary block B spanning M periods can be written explicitly as

$$B = b_1^\top \times b_2 = \underbrace{[\mathbf{1}(K_1, N_1), \mathbf{0}(K_1, N_0), \mathbf{1}(K_1, N_1), \mathbf{0}(K_1, N_0), \dots, \mathbf{1}(K_1, N_1)]}_{\text{spanning } M \text{ periods}}, \quad (33)$$

which is concatenating of M all-1's blocks and $M - 1$ all-0's blocks intervally. For instance, when $M = 4$, $K_1 = 4$, $N_0 = 4$ and $N_1 = 2$, the block B is a binary grid illustrated in Figure 2.

From (33) we can derive that the two-dimensional binary-weight block $B \in \mathbb{R}^{K_1 \times K_2}$ has a size determined by K_1 and

$$K_2 = (N_0 + N_1) \times (M - 1) + N_1. \quad (34)$$

Using B in the objective function of (27), the regularization term groups a 2-D structure of STFT coefficients with the respect to the periodicity information of x in (1).

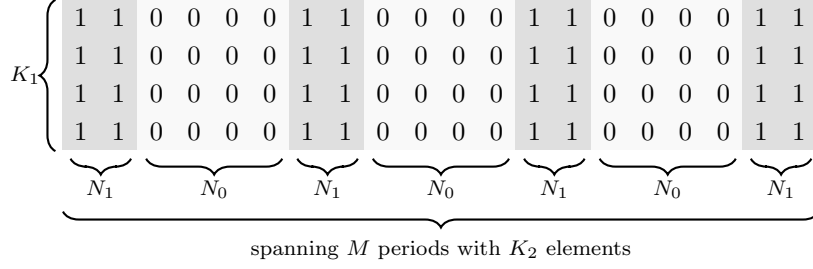


Figure 2: Example of binary block B when $M = 4$, $K_1 = 4$, $N_0 = 4$ and $N_1 = 2$.

4.3 Algorithm derivation

To solve the optimization problem (27), we split the variable c by introducing an extra equality constraint, and solve the equivalent problem

$$\{c^*, u^*\} = \arg \min_{c, u} P_0(c) + P_1(u) \quad (35a)$$

$$\text{subject to } c - u = 0 \quad (35b)$$

where $P_0 : \mathbb{C}^{M_1 \times M_2} \rightarrow \mathbb{R}$ and $P_1 : \mathbb{C}^{M_1 \times M_2} \rightarrow \mathbb{R}$ are defined as,

$$P_0(c) := \frac{1}{2} \|y - Ac\|_2^2 \quad (36a)$$

$$P_1(u) := \lambda \sum_{m_1} \sum_{m_2} \phi_\epsilon(\theta(u, B, m_1, m_2); a), \quad (36b)$$

which leads to a same solution by $c = u$ to problem (27).

The majorizer of P_1 in (35) can be found by $g(u, v)$ in (25) as,

$$G_1(u, v) = \lambda \sum_{m_1} \sum_{m_2} g(\theta(u, B, m_1, m_2), \theta(v, B, m_1, m_2)) \quad (37a)$$

$$= \lambda \sum_{m_1} \sum_{m_2} g(\|B \odot S(u, m_1, m_2)\|_2, \|B \odot S(v, m_1, m_2)\|_2) \quad (37b)$$

$$= \frac{\lambda}{2} \sum_{m_1} \sum_{m_2} [r(v)]_{m_1, m_2} [u]_{m_1, m_2}^2 + C \quad (37c)$$

where C is a constant, and $r(v) \in \mathbb{R}^{M_1 \times M_2}$ is a matrix having an explicit form

$$[r(v)]_{m_1, m_2} = \sum_{k_1=0}^{K_1-1} \sum_{k_2=0}^{K_2-1} \frac{[B]_{k_1, k_2}^2}{\psi(\|B \odot S(v, m_1 - k_1, m_2 - k_2)\|_2)}. \quad (38)$$

Then using SALMA (Theorem 1), problem (27) can be solved iteratively by

$$u^{(i+1)} = \arg \min_u G_1(u, u^{(i)}) + \frac{\mu}{2} \|u - c - d\|_2^2 \quad (39a)$$

$$c^{(i+1)} = \arg \min_c P_0(c) + \frac{\mu}{2} \|u - c - d\|_2^2 \quad (39b)$$

$$d^{(i+1)} = d^{(i)} - (u - c). \quad (39c)$$

4.3.1 Sub-problem (39a)

The step (39a) can be written as

$$u = \arg \min_u G_1(u, v) + \frac{\mu}{2} \|u - c - d\|_2^2 \quad (40)$$

where $G_1(u, v)$ is given by (37), therefore the problem has a more explicit formulation

$$u = \arg \min_u \frac{\mu}{2} \|u - (c + d)\|_2^2 + \frac{\lambda}{2} \sum_{m_1} \sum_{m_2} [r(v)]_{m_1, m_2} [u]_{m_1, m_2}^2, \quad (41)$$

which is a least square problem with explicit solution

$$u = (c + d) ./ \left[1 + \frac{\lambda [r(v)]}{\mu} \right], \quad (42)$$

where $./$ denotes the point-wise division.

4.3.2 Sub-problem (39b)

The sub-problem (39b) can be written as

$$c = \arg \min_c \frac{1}{2} \|y - Ac\|_2^2 + \frac{\mu}{2} \|u - c - d\|_2^2 \quad (43)$$

which is also a least-square problem, and it has an explicit solution

$$c = [A^H A + \mu I]^{-1} [A^H y + \mu(u - d)]. \quad (44)$$

The operator A^H is the complex conjugate transpose (Hermitian) of A . Note that to compute c by (44) we need to solve an inverse system $[A^H A + \mu I]^{-1}$. To overcome the computational cost, we use the matrix inverse lemma (see the formulation in Appendix A),

$$[A^H A + \mu I]^{-1} = \frac{1}{\mu} \left\{ I - A^H [\mu I + A A^H]^{-1} A \right\} \quad (45a)$$

$$= \frac{1}{\mu} \left[I - \frac{1}{\mu + 1} A^H A \right], \quad (45b)$$

where since the operators A^H and A here are the forward and inverse STFT, where $x = A A^H x$, then the property

$$A A^H = I \quad (46)$$

holds. As a consequence, equation (44) can be written as,

$$c = \frac{1}{\mu} \left[I - \frac{1}{\mu + 1} A^H A \right] [A^H y + \mu(u - d)] \quad (47a)$$

$$= \frac{1}{\mu} A^H y + (u - d) - \frac{1}{\mu(\mu + 1)} A^H y - \frac{1}{1 + \mu} A^H A (u - d) \quad (47b)$$

$$= (u - d) + \frac{1}{\mu + 1} A^H [y - A(u - d)], \quad (47c)$$

which is equivalent to (44), but does not require solving a linear system in (44).

Using the results derived in (42) and (47), which solve the problems (39a) and (39b) respectively, the algorithm (39) has explicit solutions of each step,

$$u^{(i+1)} = (c + d) ./ \left[1 + \frac{\lambda r(u^{(i)})}{\mu} \right] \quad (48a)$$

$$c^{(i+1)} = (u - d) + \frac{1}{\mu + 1} A^H \left[y - A(u - d) \right] \quad (48b)$$

$$d^{(i+1)} = d^{(i)} - (u - c). \quad (48c)$$

The entire algorithm to solve problem (27) is summarized in Table 3. Note that although the variables $u, c, d \in \mathbb{C}^{M_1 \times M_2}$ in the algorithm are all 2-D complex-valued matrices, in fact this does not affect the feasibility of SALMA. In each step of the algorithm (Table 3), the real and imaginary parts can be computed parallelly and separately, using real-valued expressions. More specifically, it is equivalent to implement the algorithm using 3-D matrices on $\mathbb{R}^{M_1 \times M_2 \times 2}$, and each step leads to a same result. Hence, SALMA (Theorem 1) defined in real domain, is still valid to solve the problem (27) (see Appendix B for more details).

Table 3: Solving problem (27) with SALMA.

<p>initial: $c, u, d \in \mathbb{C}^{M_1 \times M_2}, \mu > 0,$ repeat:</p> $[r]_{m_1, m_2} = \sum_{k_1} \sum_{k_2} \frac{[B]_{k_1, k_2}^2}{\psi(\ B \odot S(u, m_1 - k_1, m_2 - k_2)\ _2)}$ $u = (c + d) ./ \left[1 + \frac{\lambda}{\mu} r \right]$ $c = (u - d) + \frac{1}{\mu + 1} A^H \left[y - A(u - d) \right]$ $d = d - (u - c)$ <p>end return: $c, x = Ac.$</p>

5 Simulated data example

5.1 Example 1

We apply the proposed method to the simulated data illustrated in Figure 3(a). The simulated data is a 0.25 second signal with sampling rate $f_s = 16$ kHz. We simulate the vibration features caused by fault as a transient containing two oscillation components at 1 kHz and 2 kHz. Each transient lasts for about 4 milliseconds with a random amplitude within a range, and the two oscillatory components in one transient have independently random initial phases. The detail of a simulated oscillatory fault is shown in Figure 3(a) (inside the dashed line box). The clean data shown in Figure 3(a) is a sequence of the simulated faults with a period $T = 10$ milliseconds. Note that since each transient has a random phase, in Figure 3(a), each

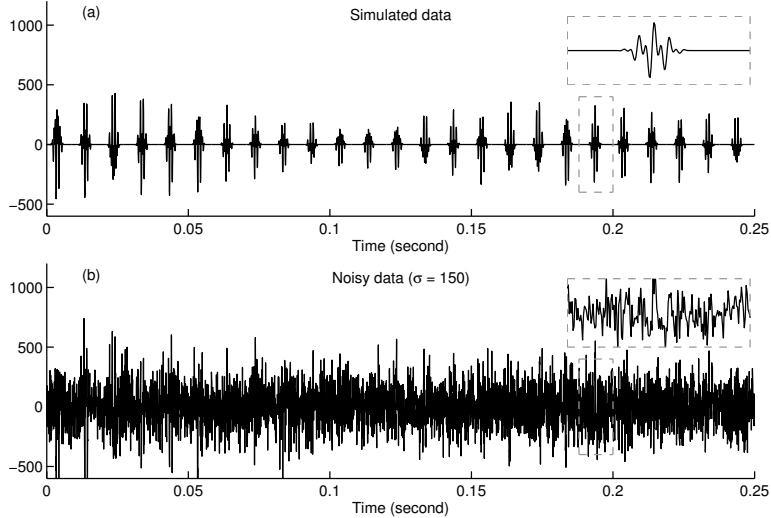


Figure 3: (a) Simulated signal, and (b) noisy observation.

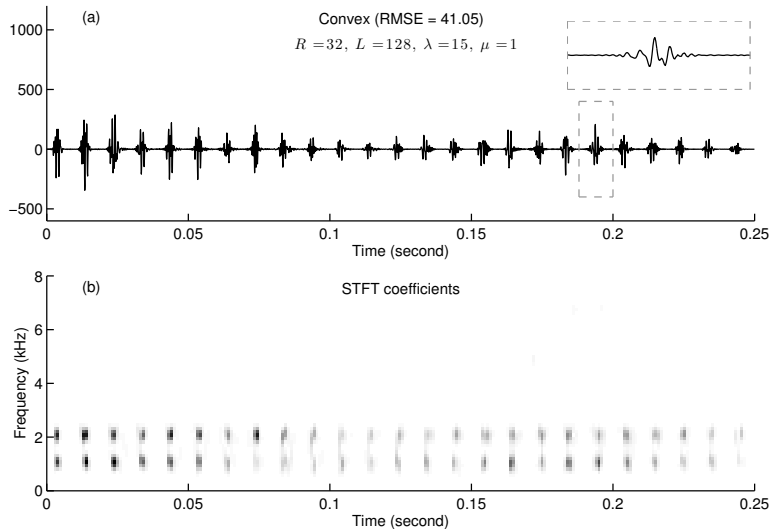


Figure 4: Result from convex penalty function, (a) estimated time domain signal, (b) STFT coefficients.

transient is different than the others. We add heavy noise to the test data, and the noisy signal is shown in Figure 3(b).

In this example, we set the STFT to have a window size $R = 32$ with 50% window overlapping, and the length of Fourier transform is $L = 256$. We can establish the block B in problem (27) by a condition of b_2 in (32) using the periodicity information, where the length of one period in the STFT domain is

$$\frac{2Tf_s}{R} \approx N_0 + N_1. \quad (50)$$

In this example, we set $K_1 = N_1 = 2$, and $N_0 + N_1 = 2Tf_s/R = 10$, and b_2 as a binary weight vector is spanning $M = 4$ periods. Hence, by (34), the size of binary weight block B is 2×32 . When using (33) to express the block, B consists of four blocks with 2×2 ones and three blocks with 2×8 zeros.

Figure 4 shows the results obtained using the proposed method with convex (smoothed ℓ_1 -norm) penalty function. Figure 4(a) is the estimated \hat{x} calculated from the STFT coefficients in Figure 4(b). The proposed

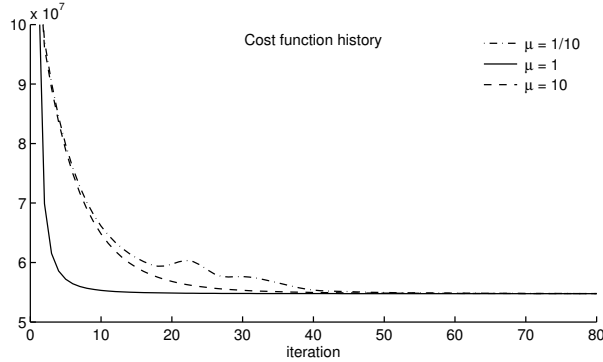


Figure 5: Converging history of using different μ 's.

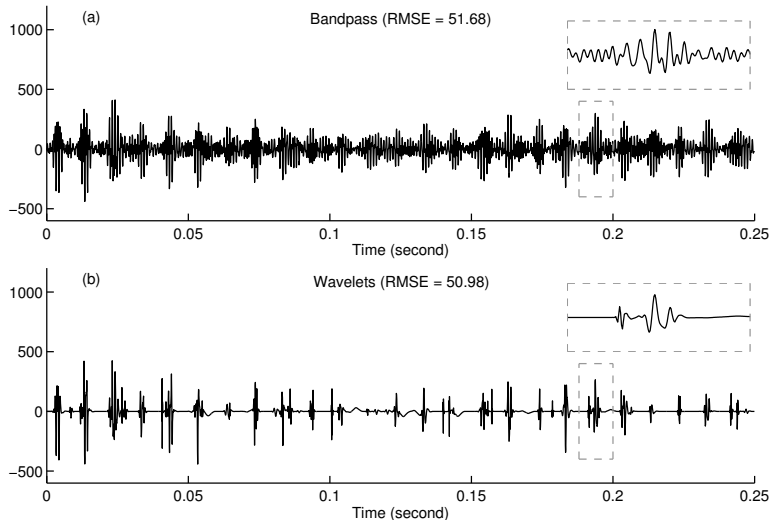


Figure 6: Denoising results of (a) bandpass filtering, (b) wavelet-based denoising.

method recovers the oscillatory transients at accurate time and frequency. Although the amplitude of the estimated \hat{x} is slightly diminished, all the ‘fault features’ (transients) are recovered at accurate locations, and in Figure 4(b), a grid of sparse blocks is distributed at the correct frequencies (about 1 and 2 kHz). In this example, we set $\lambda = 15$. Note that, similar to SALSA, the proposed method requires a parameter $\mu > 0$ which effects the convergence rate. We use several values of μ for this example, the comparison of convergence speed is shown in Figure 5. Through numerical experiments, we find that setting $\mu = 1$ gives a reasonable convergence rate, not only in this example, but also for the applications illustrated in the following sections.

For comparison, we utilize bandpass filtering. Bandpass filtering is a conventional and effective method in fault diagnosis field to extract oscillatory features or emphasize specific frequency components, and is used in conjunction with some other techniques [32, 60, 52, 16]. For instance, in [60], the author uses bandpass filtering after removing detected harmonics, and in [52, 53], the author demodulates vibration signals at characteristic frequency after using specially designed bandpass filters as pre-processing, and in [16], bandpass filtering is used as a pre-processing for a singular value decomposition (SVD) based analysis.

In this example, we use two third-order Butterworth bandpass filters with center frequencies at 1 kHz and 2 kHz respectively with ‘forward-backward’ zero-phase filtering, and the passband is about 400 Hz for both filters. Because the the passbands of the two filters do not overlap, we simply add the output signals from

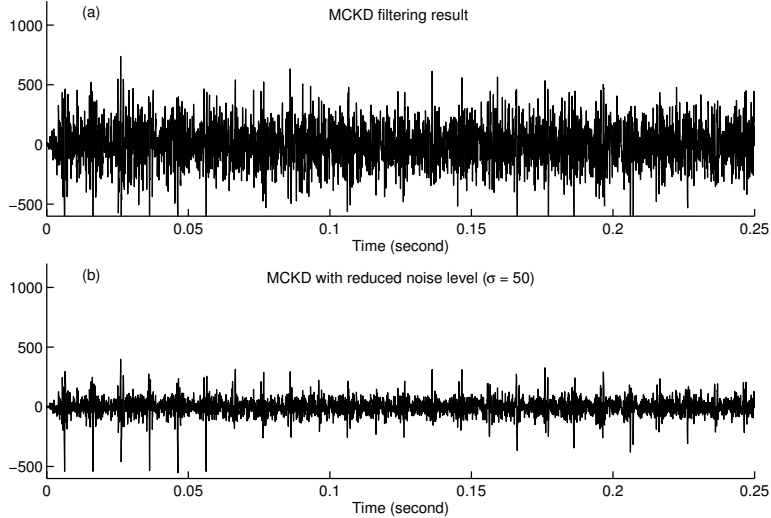


Figure 7: Filtering result using MCKD of (a) test data, (b) test data with a reduced noise level.

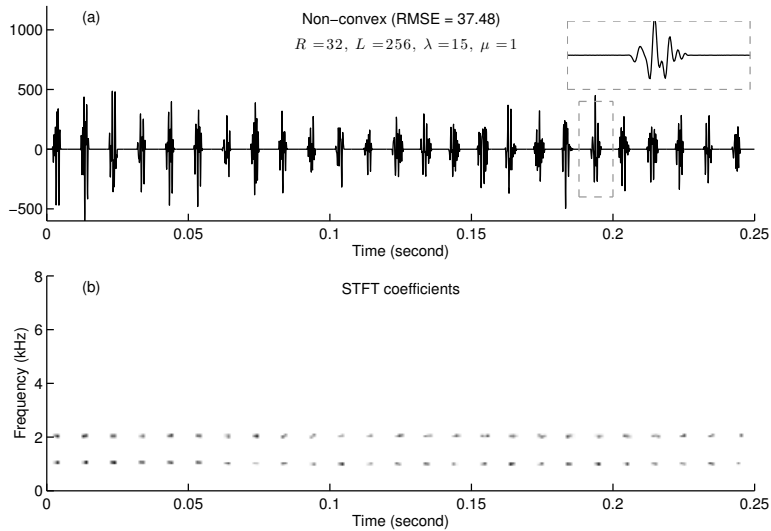


Figure 8: Enhanced result using non-convex penalty function, (a) estimated time domain signal, (b) STFT coefficients.

these two filters, and the result is shown in Figure 6(a). This result shows that linear time-invariant (LTI) filtering technique hardly recovers a zero baseline. Moreover, although some transients with large amplitude can be visually distinguished in Figure 6(a), it is hard to distinguish the transients with small amplitudes, e.g., at about $t = 0.08$ to 0.12 second. Furthermore, the result in Figure 6(a) is obtained by knowing the oscillatory frequencies exactly, but in practice, especially in the area of fault diagnosis, it is rarely possible. In this example, even though we use the accurate frequencies as prior-knowledge for the bandpass filters, the proposed method still attains a significantly better root-mean-square error (RMSE) value.

Wavelet-based denoising has also been used to extracted fault features [62, 64, 1, 39]. In this example, we adopt a conventional wavelet-coefficient thresholding method to denoise the test signal. More specifically, a 5-scale undecimated wavelet transform [15, 36] with 3 vanishing moments is used, and the result is shown in Figure 6(b). For denoising, we apply hard-thresholding and chose the threshold value by 3σ -rule for each subband. In Figure 6(b), although some large amplitude transients can be recovered at correct locations, they lose the oscillatory structure, where most recovered transients have irregular waveforms [see the cropped

example inside the dashed line box in Figure 6(b)]. In the time range from about 0.10 to 0.13 seconds, the transients are almost completely diminished.

As an application of fault diagnosis, we apply maximum correlated Kurtosis deconvolution (MCKD) [44] to the test data¹. This method deconvolves the signal from an estimated FIR filter that maximizes the correlated Kurtosis value locally. It requires the period of potential fault features. To proceed with the algorithm, we set the period length to be the true period (160 samples), and the FIR filter length to be 100, and the M-shift value to be 5 as suggested in the Matlab implementation available online. The result of MCKD is shown in Figure 7(a), where we found that the algorithm is not able to give a deconvolution result that properly indicates most of the fault features at the noise level of our test signal. When comparing to the noisy data in Figure 3(b), we can see the algorithm mistakenly promotes the impulsive features in noise. When we reduce the noise level, the algorithm is capable to properly indicate periodic fault features as promoted impulses after deconvolution. In Figure 7(b), we show an example of applying MCKD to the data in Figure 3(b), but with a reduced noise level from $\sigma = 150$ to 50.

5.2 Enhancement by non-convex penalty

Non-convex penalty functions can be utilized to further enhance the effectiveness of our proposed formulation. When the objective function (27) has a non-convex regularizer, the problem is generally non-convex, and when minimizing a non-convex function, the algorithm may get trapped in a local minima. To reduce this problem, we use the solution from the convex formulation to initialize the algorithm. Through numerical experiments, we suggest a range of values for parameter a , which controls the ‘non-convexity’ of the penalty functions in Table 2,

$$0 \leq a \leq \frac{1}{\lambda K}, \quad K = \sum_{k_1, k_2} [B]_{k_1, k_2}, \quad (51)$$

where K is also the number of 1’s when we restrict B to be a binary block as (33). This range does not guarantee the problem is convex, but in practice, using the non-convex penalty regularizers in this range significantly enhances the result and gives a stable convergence behavior.

To further reduce the problem of local minima, we can gradually increase the parameter a to its maximum value. For instance, when the upper bound of a is 0.025 in (51), we can run the algorithm (in Table 3) starting with $a = 0$ obtaining a result with convex penalty function, and then run the algorithm with non-convex penalty function five more times initialized by previous iteration, gradually increasing a by 0.05 each time. This simultaneously helps to restrict the non-convex solution close to the convex solution and promote stronger sparsity.

In this example, we use the arctangent function (‘atan’ in Table 2), and the result is shown in Figure 8(a). There is a significant improvement reflected by the RMSE value compared to the convex penalty function in Figure 4. We also show the absolute value of STFT coefficients in Figure 8(b), a significant enhanced sparsity in the STFT domain can be seen.

¹Matlab implementation is available online: <http://www.mathworks.com/matlabcentral/fileexchange/31326-maximum-correlated-kurtosis-deconvolution--mckd->

Table 4: Defect frequencies of drive end bearing (multiple by running speed)

Inner race	Outer race	Cage train	Rolling element
5.4152	3.5848	0.39828	4.7135

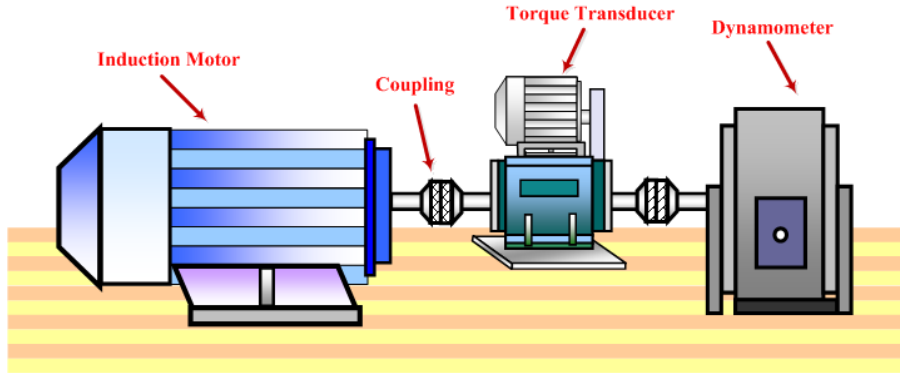


Figure 9: Example 2: Test stand for vibration monitoring.

6 Experiment and engineering validation

In this section, we illustrate the proposed method by applying it to data recorded from two different machines. One is from a public dataset concerning bearing faults. The other data was collected by State Key Laboratory for Manufacturing and Systems Engineering of Xi’an Jiaotong University for fault diagnosis of gearbox [8].

6.1 Example 2: experimental data validation

In this example, we utilized the proposed method to detect potential inner race fault of the drive end bearing from an experimental setup. The experimental vibration data was acquired from the Case Western Reserve University Bearing Data Center².

As shown in Figure 9, the test stand consists of a 2 hp motor (left), a torque transducer/encoder (center), and a dynamometer (right). The bearing installed on the drive end is a 6205-2RS-JEM SKF deep-groove ball bearing. The potential defect frequencies of drive end bearing are listed in Table 4, dependent on the location of the fault. More details about the experiment setup can be found at the website <http://csegroups.case.edu/bearingdatacenter/pages/apparatus-procedures>.

A measured vibration signal is shown in Figure 10(a), with a sampling rate $f_s = 12$ kHz. The signal was collected using accelerometers, which were attached to the housing with magnetic bases. The current rotational speed of the motor is approximately 1730 r/min. Thus, according to Table 4, the fault characteristic frequency of the drive end bearing inner race is about $f_i = 1730/60 \times 5.4152 \approx 156$ Hz. To run the proposed algorithm, we set the STFT window length to $R = 16$ samples, and the number of the frequency bins to 512 for each window. For the binary block in the STFT domain, we set that each block spans $M = 4$ periods, and $K_1 = 2$, $N_1 = 2$, then the block B can be determined by (32), (33) and (50).

In order to validate the reliability of the proposed algorithm, we also test it on a normal (no fault) setup under the same rotation speed. The test signal is shown in Figure 11(a), and using the same parameters, there is no oscillatory feature extracted, and the output of the proposed method is almost zero [see Figure 11(b)].

To achieve a more visualizable oscillatory feature detection signal, we sum the absolute values of STFT

²Available online: <http://csegroups.case.edu/bearingdatacenter/pages/download-data-file>

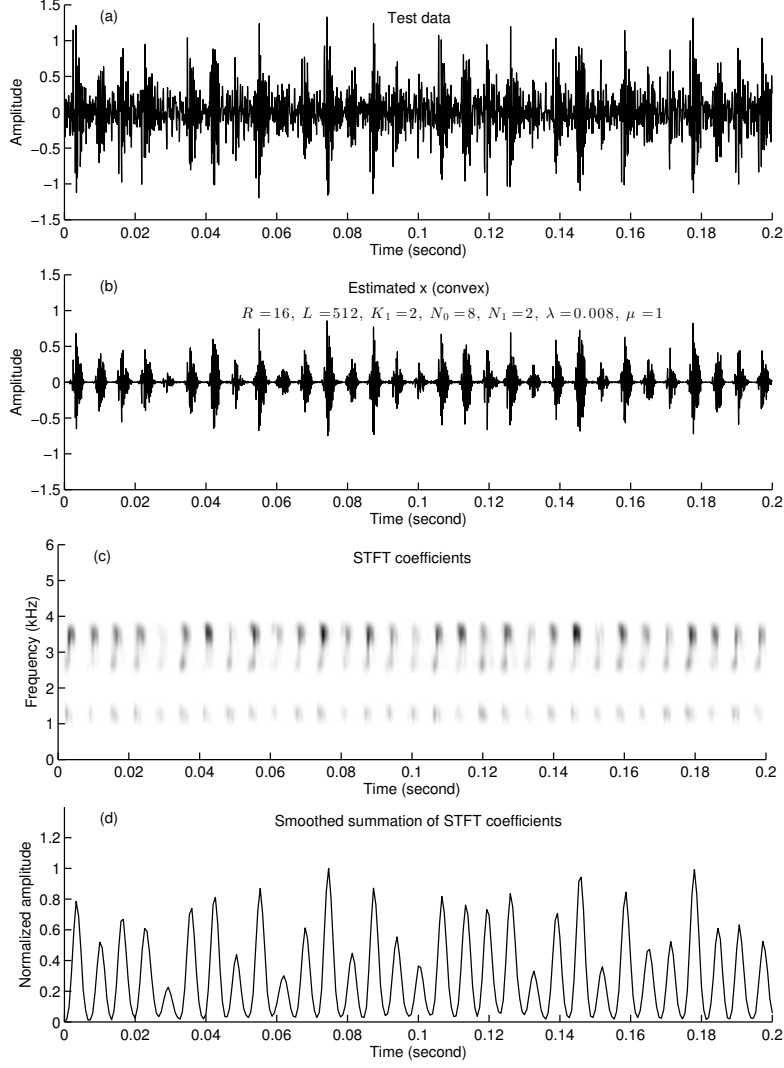


Figure 10: Example 2: (a) test data, (b) estimated signal, (c) STFT coefficients, (d) smoothed profile.

coefficients c^* through frequency domain, and then the obtained result is lowpass filtered,

$$s(m_2) = \text{LPF} \left\{ \sum_{m_1} |[c^*]_{m_1, m_2}| \right\}, \quad (52)$$

where m_1 denotes the frequency index and LPF denotes a lowpass filter. Then we can obtain a smooth time series $s \in \mathbb{R}^{M_2}$, indicating the time and strength of extracted oscillatory features caused by faults [see Figure 10(c)]. For comparison, we utilize fast spectral kurtosis (SK) [4, 3]³ to analyze the same vibration data. This method extracts the ‘envelope spectrum’ of the optimal subband indicating potential fault features. The Kurtogram and the envelope spectrum of the optimal subband is shown in Figure 12, where we use the optimal subband SK detected automatically at 3 kHz and level 2.2. In Figure 12(b) the large spikes indicate the fault features. The profile in Figure 10(d) more clearly indicates the fault features than the one in Figure 12(b). We can apply lowpass filtering to the ‘noisy’ envelop extracted by SK as well,

³Matlab implementation is available online: <http://www.mathworks.com/matlabcentral/fileexchange/48912-fast-kurtogram>

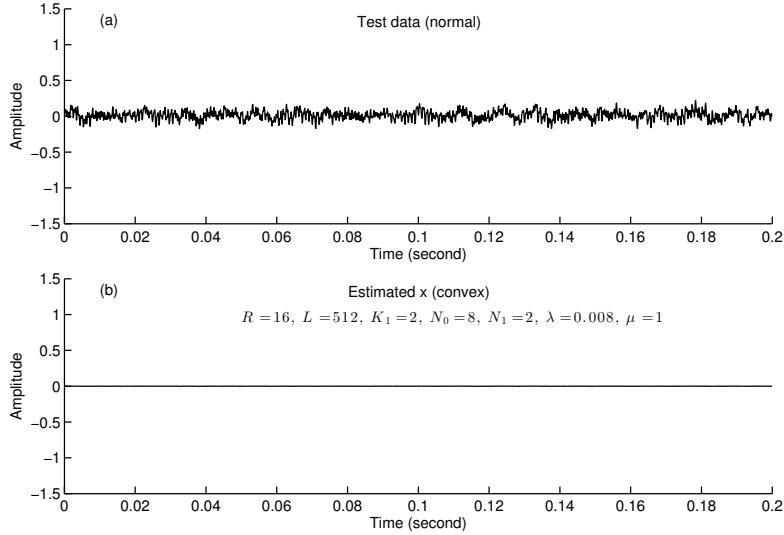


Figure 11: Example 2: (a) test data of normal setup, (b) estimated signal

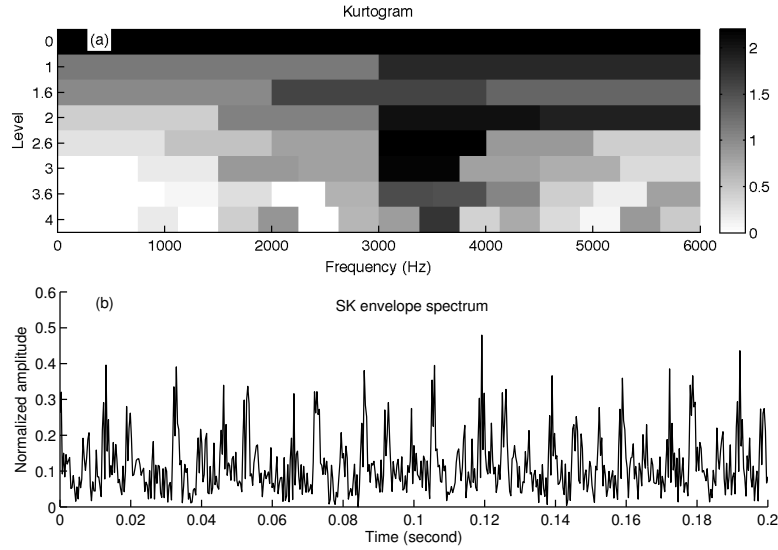


Figure 12: Example 2: (a) Kurtogram, (b) envelop spectrum.

but in this case, it tends to eliminate some spikes with small amplitudes, such as the one at about $t = 0.03$ second.

6.2 Example 3: rub-impact fault detection in the gearbox of an oil refinery

In this engineering application, we applied the proposed method to detect a rub-impact fault developed in the gearbox of an oil refinery to further verify its effectiveness. One large oxygen separation and compression unit of this oil refinery was operating with severely abnormal sounds after an overhaul and thus suspected to have faults induced in its components.

The schematic of the oxygen separation and compression unit is illustrated in Figure 13. The characteristic frequencies of interest are listed in Table 5. The sampling frequency of the acquired vibration signals is 15 kHz, and each epoch of signal is of length 1024. One acceleration signal measured from a sensor and its Fourier spectrum are displayed in Figure 15(a) and Figure 15(b), respectively. Peak frequencies of 1479 Hz,

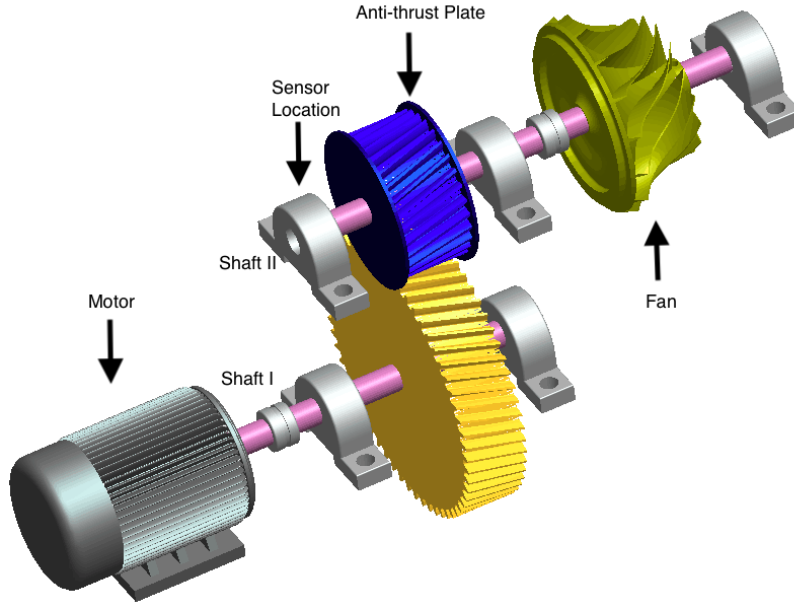


Figure 13: Example 2: Schematic of the oxygen separation and the sensor location.

Table 5: The relevant characteristic frequencies of oxygen separation and compression unit

Rotating speed of motor (r/m)	2985
Rotating frequency of shaft I (Hz)	49.75
Rotating frequency of shaft II (Hz)	213
Meshing frequency of gearbox (Hz)	6815.75
Rotating frequency of fan blades (Hz)	3620.86/4472.83

2947 Hz, and 4219 Hz can be observed in Figure 15(b). In addition, the peak frequencies are all surrounded by sidebands spaced at about 213 Hz. Note that 213 Hz exactly corresponds to the rotating frequency of shaft II, as shown in Table 5. Thus, the rotating frequency of shaft II ($f_2 = 213$ Hz) can be utilized as prior knowledge of fault features.

In the practical shutdown inspection, a rub-impact fault between the end face of the anti-thrust plate on the pinion and that of the bull gear was found. The fault was due to the inappropriate installation of the pinion [8]. The end face of the anti-thrust plate and that of the bull gear were not strictly parallel due to non-perpendicularity between the pinion and Shaft II. Figure 14 illustrates the rubbing fault occurred between the end face of the anti-thrust plate on the pinion and that of the bull gear.

In order to capture the potential fault feature in Shaft II, the formula (50) is implemented with $T = 1/f_2$ to build the binary weight block (33). More specifically, in this example, we set $M = 4$, $K_1 = 2$, $N_1 = 2$, and $N_0 + N_1 = 9$, to establish the the binary weight block B with (32) and (33). Figure 16 shows the result using proposed method with non-convex ('atan') penalty function, where a periodic sequence of oscillatory transients is obtained with a baseline almost zero. In the STFT domain, a sequence of periodic clusters can be observed at about 4 kHz, which coincides to the peak signature frequency around 4 kHz in Figure 15(b). The proposed method not only extracts the periodic oscillatory fault features, but also gives the oscillation frequency precisely.

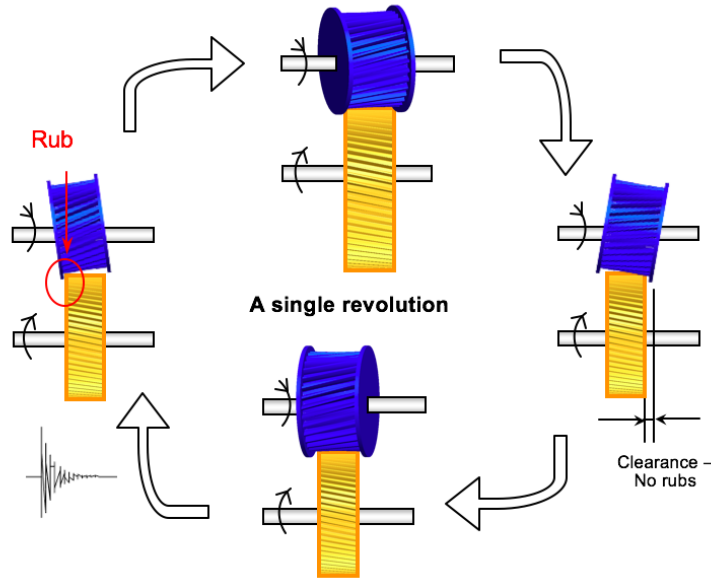


Figure 14: Example 3: Illustration of rub-impact between the end face of the anti-thrust plate on the pinion and that of the bull gear.

7 Conclusion

This paper proposes an approach using structured sparsity in the STFT domain to extract oscillatory features caused by faults in rotating machinery. We model the feature caused by a potential fault as a quasi-periodic sequence of oscillatory transients, where each transient may contain multiple consistent frequency components. The proposed approach uses smoothed (convex or non-convex) penalty functions to promote the sparsity of specially grouped STFT domain coefficients in an optimization problem. This approach detects sparse and periodically distributed coefficients, and the periodically oscillatory fault features can be extracted. Using the estimated STFT coefficients, the signature frequency of the fault feature can be directly observed due to the nature of sparsity in the time-frequency domain. To solve the proposed optimization problem efficiently, an iterative algorithm which combines majorization-minimization and split augmented Lagrangian shrinkage algorithm has been illustrated. When the problem is not convex, this algorithm still converges to a local optimum. The effectiveness of the proposed approach is verified by simulation data, experimental data, and engineering data. The results demonstrate the notable effectiveness of the proposed approach in extracting transients for detecting faults in rotating machines.

A Matrix inverse lemma

The matrix inverse lemma has several forms. A common form is

$$(A + BD^{-1}C)^{-1} = A^{-1} - A^{-1}B(D + CA^{-1}B)^{-1}CA^{-1}. \quad (53)$$

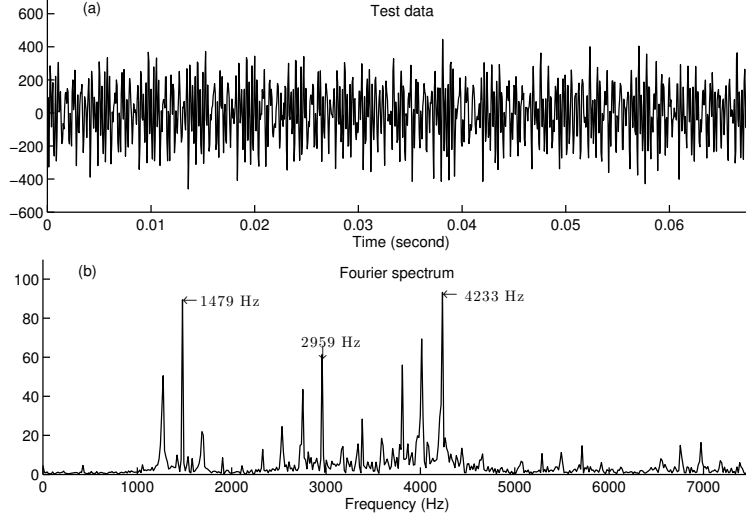


Figure 15: Example 3: (a) measured test data. (b) frequency domain.

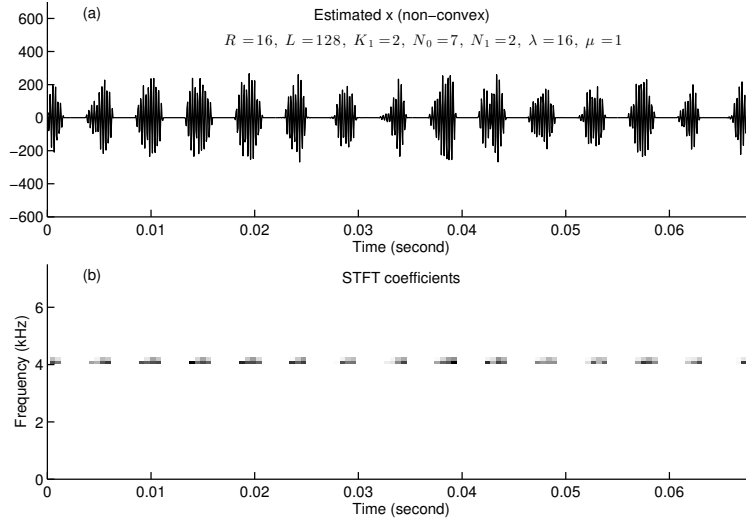


Figure 16: Example 3: Result using non-convex penalty function, (a) estimated time domain signal, (b) STFT coefficients.

B Equivalent formulation of real values

To rewrite the algorithm into real value formulation, we consider the complex variables as an extended real value array, such that

$$\bar{c} = \begin{bmatrix} c_r \\ c_i \end{bmatrix} = \begin{bmatrix} \text{Re}(c) \\ \text{Im}(c) \end{bmatrix} \in \mathbb{R}^{M_1 \times M_2 \times 2}, \quad (54)$$

and correspondingly the original variable c can be recovered by $c = c_r + c_i i$. Additionally, to facilitate further derivations, we also define all the other complex variables into a formulation of real values,

$$\bar{u} = \begin{bmatrix} u_r \\ u_i \end{bmatrix}, \quad \bar{d} = \begin{bmatrix} d_r \\ d_i \end{bmatrix}, \quad \bar{v} = \begin{bmatrix} v_r \\ v_i \end{bmatrix}. \quad (55)$$

Moreover, we also consider the short-time Fourier transform operator A^H and its inverse operator A in (27) into a formulation that works on real domain. We define $\bar{A} : \mathbb{R}^{M_1 \times M_2 \times 2} \rightarrow \mathbb{R}^N$ is a operator working equivalently to A when realigning c as \bar{c} in (54), where

$$\bar{A}\bar{c} = x, \quad (56)$$

and its inverse is to do the transform and then align the real and imaginary parts of the output,

$$\bar{A}^\top x = \begin{bmatrix} \text{Re}(A^H x) \\ \text{Im}(A^H x) \end{bmatrix}, \quad (57)$$

Hence, the property (46) is still persevered as $\bar{A}\bar{A}^\top = I$. As a consequence, solving the problem sequence (39) is equivalent to compute the following steps,

$$u^{(i+1)} = \begin{cases} \bar{u}^{(i+1)} = (\bar{c} + \bar{d}) ./ \left[1 + \frac{\lambda \bar{r}(\bar{u}^{(i)})}{\mu} \right] \\ u^{(i+1)} = u_r^{(i+1)} + i u_i^{(i+1)} \end{cases} \quad (58a)$$

$$c^{(i+1)} = \begin{cases} \bar{c}^{(i+1)} = (\bar{u} - \bar{d}) + \frac{1}{\mu + 1} \bar{A}^\top \left[y - \bar{A}(\bar{u} - \bar{d}) \right] \\ c^{(i+1)} = c_r^{(i+1)} + i c_i^{(i+1)} \end{cases} \quad (58b)$$

$$d^{(i+1)} = \begin{cases} \bar{d}^{(i+1)} = \bar{d}^{(i)} - (\bar{u} - \bar{c}) \\ d^{(i+1)} = d_r^{(i+1)} + i d_i^{(i+1)} \end{cases} \quad (58c)$$

where $\bar{r}(\bar{v}) \in \mathbb{R}^{M_1 \times M_2 \times 2}$ in (58a) is defined as

$$[\bar{r}(\bar{v})]_{m_1, m_2, j} = \sum_{k_1=0}^{K_1-1} \sum_{k_2=0}^{K_2-1} \frac{[B]_{k_1, k_2}^2}{\psi(p(\bar{v}, B, m_1 - k_1, m_2 - k_2))}, \quad \text{for } j = 1, 2. \quad (59)$$

where

$$p(\bar{v}, B, j_1, j_2) = \left[\|B \odot S(v_r, j_1, j_2)\|_2^2 + \|B \odot S(v_i, j_1, j_2)\|_2^2 \right]^{1/2}. \quad (60)$$

Note that when comparing (38) to (59),

$$[\bar{r}(\bar{v})]_{m_1, m_2, j} = [r(v)]_{m_1, m_2}, \quad \text{for } j = 1, 2. \quad (61)$$

Therefore, each step of (48) can be understood as computing corresponding real and imaginary parts as real values, and then recovering the corresponding complex results afterwards. When we denote the steps on complex domain as (48), it does not affect the independency of real and imaginary parts. Hence, the convergence of using SALMA for this problem is ensured as each step solved on real domain with proper vectorization equivalently.

References

- [1] S. Abbasion, A. Rafsanjani, A. Farshidianfar, and N. Irani. Rolling element bearings multi-fault classification based on the wavelet denoising and support vector machine. *Mech. Syst. Signal Process.*, 21(7):2933–2945, October 2007.
- [2] M. V. Afonso, J. M. Bioucas-Dias, and M. A. T. Figueiredo. Fast image recovery using variable splitting and constrained optimization. *IEEE Trans. Image Process.*, 19(9):2345–2356, September 2010.
- [3] J. Antoni. Fast computation of the kurtogram for the detection of transient faults. *Mech. Syst. Signal Process.*, 21(1):108–124, January 2007.
- [4] J. Antoni and R. B. Randall. The spectral kurtosis: application to the vibratory surveillance and diagnostics of rotating machines. *Mech. Syst. Signal Process.*, 20(2):308–331, February 2006.
- [5] A. Beck and L. Tetruashvili. On the convergence of block coordinate descent type methods. *SIAM Journal on Optimization*, 23(4):2037–2060, 2013.
- [6] S. Boyd, N. Parikh, E. Chu, B. Peleato, and J. Eckstein. Distributed optimization and statistical learning via the alternating direction method of multipliers. *Foundations and Trends in Machine Learning*, 3(1):1–122, 2011.
- [7] I. S. Bozchalooi and M. Liang. A smoothness index-guided approach to wavelet parameter selection in signal de-noising and fault detection. *J. Sound Vib.*, 308(12):246–267, November 2007.
- [8] B. Chen, Z. Zhang, C. Sun, B. Li, Y. Zi, and Z. He. Fault feature extraction of gearbox by using overcomplete rational dilation discrete wavelet transform on signals measured from vibration sensors. *Mech. Syst. Signal Process.*, 33:275–298, November 2012.
- [9] B. Chen, Z. Zhang, Y. Zi, Z. He, and C. Sun. Detecting of transient vibration signatures using an improved fast spatial-spectral ensemble kurtosis kurtogram and its applications to mechanical signature analysis of short duration data from rotating machinery. *Mech. Syst. Signal Process.*, 40(1):1–37, October 2013.
- [10] P.-Y. Chen and I. W. Selesnick. Group-sparse signal denoising: Non-convex regularization, convex optimization. *IEEE Trans. Signal Process.*, 62(13):3464–3478, July 2014.
- [11] P.-Y. Chen and I. W. Selesnick. Translation-invariant shrinkage/thresholding of group sparse signals. *Signal Processing*, 94:476–489, 2014.
- [12] S. Chen and D. L. Donoho. Basis pursuit. In *1994 Conference Record of the Twenty-Eighth Asilomar, Conference on Signals, Systems and Computers, 1994.*, volume 1, pages 41–44, October 1994.
- [13] S. Chen, D. L. Donoho, and M. A. Saunders. Atomic decomposition by basis pursuit. *SIAM J. Sci. Comput.*, 20(1):33–61, 1998.
- [14] T. W. S. Chow and F. Gou. Three phase induction machines asymmetrical faults identification using bispectrum. *IEEE Trans. Energy Conversion*, 10(4):688–693, December 1995.
- [15] R. R. Coifman and D. L. Donoho. Translation-invariant de-noising. In *Wavelet and statistics*, pages 125–150. Springer-Verlag, 1995.

- [16] F. Cong, W. Zhong, S. Tong, N. Tang, and J. Chen. Research of singular value decomposition based on slip matrix for rolling bearing fault diagnosis. *J. Sound Vib.*, 344(0):447–463, 2015.
- [17] L. Cui, J. Wang, and S. Lee. Matching pursuit of an adaptive impulse dictionary for bearing fault diagnosis. *J. Sound Vib.*, 333(10):2840–2862, 2014.
- [18] Y. Ding and I. W. Selesnick. Sparsity-based correction of exponential artifacts. *Signal Process.*, 120:236–248, March 2016.
- [19] J. Eckstein and D. P. Bertsekas. On the Douglas-Rachford splitting method and the proximal point algorithm for maximal monotone operators. *Math. Program.*, 55(3):293–318, June 1992.
- [20] M. El Hachemi Benbouzid. A review of induction motors signature analysis as a medium for faults detection. *IEEE Trans. Industrial Electronics*, 47(5):984–993, October 2000.
- [21] M. Elad, J. Starck, P. Querre, and D. Donoho. Simultaneous cartoon and texture image inpainting using morphological component analysis (MCA). *J. of Appl. and Comp. Harm. Analysis*, 19(3):340–358, November 2005.
- [22] Z. Feng, M. Liang, and F. Chu. Recent advances in time-frequency analysis methods for machinery fault diagnosis: A review with application examples. *Mech. Syst. Signal Process.*, 38(1):165–205, July 2013.
- [23] Z. Feng and M. J. Zuo. Vibration signal models for fault diagnosis of planetary gearboxes. *J. Sound Vib.*, 331(22):4919–4939, October 2012.
- [24] M. Figueiredo, J. Bioucas-Dias, and R. Nowak. Majorization-minimization algorithms for wavelet-based image restoration. *IEEE Trans. Image Process.*, 16(12):2980–2991, December 2007.
- [25] W. Guo and W. T. Peter. A novel signal compression method based on optimal ensemble empirical mode decomposition for bearing vibration signals. *J. Sound Vib.*, 332(2):423–441, January 2013.
- [26] Q. He. Vibration signal classification by wavelet packet energy flow manifold learning. *J. Sound Vib.*, 332(7):1881–1894, April 2013.
- [27] Q. He and X. Wang. Time-frequency manifold correlation matching for periodic fault identification in rotating machines. *J. Sound Vib.*, 332(10):2611–2626, 2013.
- [28] W. He, Y. Ding, Y. Zi, and I. W. Selesnick. Sparsity-based algorithm for detecting faults in rotating machines. Preprint, available at <http://eeweb.poly.edu/iselesni/pubs/index.html>, 2015.
- [29] W. He, Y. Zi, B. Chen, S. Wang, and Z. He. Tunable Q-factor wavelet transform denoising with neighboring coefficients and its application to rotating machinery fault diagnosis. *Sci. China Technol. Sci.*, 56(8):1956–1965, 2013.
- [30] W. He, Y. Zi, B. Chen, and Z. Wu, F. and He. Automatic fault feature extraction of mechanical anomaly on induction motor bearing using ensemble super-wavelet transform. *Mech. Syst. Signal Process.*, 54-55:457–480, March 2015.
- [31] D. R. Hunter and K. Lange. A tutorial on MM algorithms. *Amer. Statist.*, 58:30–37, 2004.

- [32] W Jiang, S. K. Spurgeon, J. A. Twiddle, F. S. Schlindwein, Y. Feng, and S. Thanagasundram. A wavelet cluster-based band-pass filtering and envelope demodulation approach with application to fault diagnosis in a dry vacuum pump. *Proc. the Institution of Mechanical Engineers, Part C: J. Mechanical Engineering Science.*, 221(11):1279–1286, 2007.
- [33] P. K. Kankar, S. C. Sharma, and S. P. Harsha. Rolling element bearing fault diagnosis using wavelet transform. *Neurocomputing*, 74(10):1638–1645, 2011.
- [34] C. Kar and A. R. Mohanty. Monitoring gear vibrations through motor current signature analysis and wavelet transform. *Mech. Syst. Signal Process.*, 20(1):158–187, 2006.
- [35] C. Kar and A. R. Mohanty. Vibration and current transient monitoring for gearbox fault detection using multiresolution fourier transform. *J. Sound Vib.*, 311(12):109–132, 2008.
- [36] M. Lang, H. Guo, J. E. Odegard, C. S. Burrus, and R. O. Wells, Jr. Noise reduction using an undecimated discrete wavelet transform. *IEEE Signal Processing Letters*, 3(1):10–12, January 1996.
- [37] K. Lange, D. Hunter, and I. Yang. Optimization transfer using surrogate objective functions. *J. of Comp. Graph. Statist.*, 9:1–20, 2000.
- [38] Y. Lei, J. Lin, Z. He, and M. J. Zuo. A review on empirical mode decomposition in fault diagnosis of rotating machinery. *Mech. Syst. Signal Process.*, 35(1):108–126, February 2013.
- [39] Z. Li, Z. He, Y. Zi, and Y. Wang. Customized wavelet denoising using intra- and inter-scale dependency for bearing fault detection. *J. Sound Vib.*, 313(12):342–359, 2008.
- [40] M. Liang and I. Soltani Bozchalooi. An energy operator approach to joint application of amplitude and frequency-demodulations for bearing fault detection. *Mech. Syst. Signal Process.*, 24(5):1473 – 1494, 2010.
- [41] M. Liang and H. Faghidi. Intelligent bearing fault detection by enhanced energy operator. *Expert Syst. Appl.*, 41(16):7223–7234, 2014.
- [42] Z. Q. Luo and P. Tseng. On the convergence of the coordinate descent method for convex differentiable minimization. *Journal of Optimization Theory and Applications*, 72(1):7–35, 1992.
- [43] S. Mallat and Z. Zhang. Matching pursuits with time-frequency dictionaries. *IEEE Trans. Signal Process.*, 41:3397–3415, December 1993.
- [44] G. L. McDonald, Q. Zhao, and M. J. Zuo. Maximum correlated kurtosis deconvolution and application on gear tooth chip fault detection. *Mech. Syst. Signal Process.*, 33(0):237–255, 2012.
- [45] X. Ning and I. W. Selesnick. ECG enhancement and QRS detection based on sparse derivatives. *Biomedical Signal Processing and Control*, 8(6):713–723, 2013.
- [46] Y. Qin, Y. Mao, and B. Tang. Vibration signal component separation by iteratively using basis pursuit and its application in mechanical fault detection. *J. Sound Vib.*, 332(20):5217–5235, 2013.
- [47] R. B Randall and J. Antoni. Rolling element bearing diagnostics – a tutorial. *Mech. Syst. Signal Process.*, 25(2):485–520, February 2011.

- [48] M. Razaviyayn, H. Baligh, A. Callard, and Z.-Q. Luo. Joint user grouping and transceiver design in a MIMO interfering broadcast channel. *IEEE Trans. Signal Process.*, 62(1):85–94, January 2014.
- [49] M. Razaviyayn, M. Hong, and Z. Luo. A unified convergence analysis of block successive minimization methods for nonsmooth optimization. *SIAM Journal on Optimization*, 23(2):1126–1153, 2013.
- [50] I. W. Selesnick. Sparse signal representations using the tunable Q-factor wavelet transform. In *Proc. SPIE*, volume 8138 (Wavelets and Sparsity XIV), 2011.
- [51] I. W. Selesnick. Wavelet transform with tunable Q-factor. *IEEE Trans. Signal Process.*, 59(8):3560–3575, August 2011.
- [52] Y.-T. Sheen. A complex filter for vibration signal demodulation in bearing defect diagnosis. *J. Sound Vib.*, 276(12):105–119, 2004.
- [53] Y.-T. Sheen. An analysis method for the vibration signal with amplitude modulation in a bearing system. *J. Sound Vib.*, 303(35):538–552, 2007.
- [54] J.-L. Starck, M. Elad, and D. Donoho. Redundant multiscale transforms and their application for morphological component analysis. *Advances in Imaging and Electron Physics*, 132:287–348, 2004.
- [55] J.-L. Starck, M. Elad, and D. Donoho. Image decomposition via the combination of sparse representation and a variational approach. *IEEE Trans. Image Process.*, 14(10):1570–1582, October 2005.
- [56] W. Su, F. Wang, H. Zhu, Z. Zhang, and Z. Guo. Rolling element bearing faults diagnosis based on optimal morlet wavelet filter and autocorrelation enhancement. *Mech. Syst. Signal Process.*, 24(5):1458–1472, 2010.
- [57] H. Tang, J. Chen, and G. Dong. Sparse representation based latent components analysis for machinery weak fault detection. *Mech. Syst. Signal Process.*, 46(2):373–388, June 2014.
- [58] D. Wang and Q. Miao. Smoothness index-guided bayesian inference for determining joint posterior probability distributions of anti-symmetric real laplace wavelet parameters for identification of different bearing faults. *J. Sound Vib.*, 345(0):250 – 266, 2015.
- [59] J. Wang and Q. He. Exchanged ridge demodulation of time-scale manifold for enhanced fault diagnosis of rotating machinery. *J. Sound Vib.*, 333(11):2450–2464, 2014.
- [60] W. Wang. Early detection of gear tooth cracking using the resonance demodulation technique. *Mech. Syst. Signal Process.*, 15(5):887–903, 2001.
- [61] R. Yan and R. X. Gao. Harmonic wavelet-based data filtering for enhanced machine defect identification. *J. Sound Vib.*, 329(15):3203–3217, July 2010.
- [62] R. Yan, R. X. Gao, and X. Chen. Wavelets for fault diagnosis of rotary machines: A review with applications. *Signal Process.*, 96:1–15, March 2014.
- [63] H. Yang, J. Mathew, and L. Ma. Fault diagnosis of rolling element bearings using basis pursuit. *Mech. Syst. Signal Process.*, 19(2):341–356, 2005.
- [64] H.-T. Yang and C.-C. Liao. A de-noising scheme for enhancing wavelet-based power quality monitoring system. *IEEE Trans. Power Delivery*, 16(3):353–360, July 2001.

- [65] Y. Zhang and R. B. Randall. Rolling element bearing fault diagnosis based on the combination of genetic algorithms and fast kurtogram. *Mech. Syst. Signal Process.*, 23(5):1509–1517, July 2009.